

Supplementary information

Multifunctional composite magnet realizing record-high transverse thermoelectric generation

Fuyuki Ando,^{*a} Takamasa Hirai,^a Abdulkareem Alasli,^b Hossein Sepehri-Amin,^a Yutaka Iwasaki,^a Hosei Nagano^b and Ken-ichi Uchida^{*ac}

^a. National Institute for Materials Science, Tsukuba 305-0047, Japan

^b. Department of Mechanical Systems Engineering, Nagoya University, Nagoya 464-8603, Japan

^c. Department of Advanced Materials Science, Graduate School of Frontier Sciences,
The University of Tokyo, Kashiwa 277-8561, Japan

*E-mail: ANDO.Fuyuki@nims.go.jp; UCHIDA.Kenichi@nims.go.jp

Note S1. Observation of nonuniform charge-to-heat current conversion in MCM

To buttress the appearance of the transverse thermoelectric conversion, we measured the charge-current-induced temperature modulation in SmCo₅/BST-based MCM by using the LIT technique. The application of \mathbf{J}_c induces a net heat current \mathbf{J}_q in the orthogonal direction by the off-diagonal Peltier effect, which is the Onsager reciprocal of ODSE.¹ We performed LIT measurements at $J_c = 1$ A and various f values in the cross-sectional and top-side configurations, as shown in Fig. S1a,b, and obtained A and φ images using Enhanced Lock-In Thermal Emission (ELITE, DCG Systems G.K.) at room temperature and atmospheric pressure. The SmCo₅/BST-based MCM with $\theta = 25^\circ$ and dimensions of $2.2 \times 11.7 \times 2.0$ mm was used for the LIT measurements. The procedures of the mounting and surface coating of the sample were the same as the experiments in Fig. 3f and Experimental section in the main text.

Fig. S1c–f shows the results of the LIT measurements. In the cross-sectional configuration, the A and φ images at $f = 10.0$ Hz indicate that alternating heating and cooling signals are localized near the SmCo₅/BST interfaces in a similar manner to that shown in Fig. 3f in the main text. Importantly, the magnitude of the A signals for $\theta = 25^\circ$ was nonuniform along the oblique interfaces because the charge current flowed nonuniformly due to the anisotropic electrical conductivity; this is the origin of transverse thermoelectric conversion by the off-diagonal Peltier effect. These local heating and cooling signals were broadened through thermal diffusion as f decreased. The A image at $f = 0.1$ Hz, showing a nearly steady-state amplitude of the temperature modulation, indicates that large temperature changes occurred near the upper and lower edges of the sample. The φ signals varied from approximately 0° (red regions) to 180° (blue regions) in the direction perpendicular to \mathbf{J}_c , indicating transverse thermoelectric heating and cooling, respectively.¹ This behavior is more evident in the results for the top-side configuration. Fig. S1e,f shows that almost uniform φ signals of approximately 180° are induced by the longitudinal charge current at $f = 0.1$ Hz, confirming that SmCo₅/BST-based MCM operates as a transverse thermoelectric converter. Fig. S1g shows the line profiles of the average temperature modulation signals in the area defined by the white dotted rectangles in Fig. S1e,f, where the A signals periodically change due to the multilayer structure. Our MCM exhibited a considerably larger temperature modulation of 1–2 K at $f = 0.1$ Hz than that in the previously reported Nd₂Fe₁₄B/Bi₈₈Sb₁₂-based ATMLs (approximately 0.2 K) with the same J_c and f values.¹ The observation of the large off-diagonal Peltier effect ensures that our MCM exhibits large transverse thermoelectric generation by ODSE.

Note S2. Calculation of thermoelectric parameters in MCM

The thermoelectric parameters, *i.e.*, electrical resistivity ρ_{ij} , thermal conductivity κ_{ij} , and thermopower S_{ij} , for SmCo₅/BST-based ATML are calculated based on Goldsmid's method as follows:

$$\rho_{xx} = \rho_{\parallel} \cos^2 \theta + \rho_{\perp} \sin^2 \theta \quad (1)$$

$$\rho_{yy} = \rho_{\parallel} \sin^2 \theta + \rho_{\perp} \cos^2 \theta \quad (2)$$

$$\rho_{xy} = (\rho_{\parallel} - \rho_{\perp}) \sin \theta \cos \theta \quad (3)$$

$$\kappa_{xx} = \kappa_{\parallel} \cos^2 \theta + \kappa_{\perp} \sin^2 \theta \quad (4)$$

$$\kappa_{yy} = \kappa_{\parallel} \sin^2 \theta + \kappa_{\perp} \cos^2 \theta \quad (5)$$

$$\kappa_{xy} = (\kappa_{\parallel} - \kappa_{\perp}) \sin \theta \cos \theta \quad (6)$$

$$S_{xx} = S_{\parallel} \cos^2 \theta + S_{\perp} \sin^2 \theta \quad (7)$$

$$S_{yy} = S_{\parallel} \sin^2 \theta + S_{\perp} \cos^2 \theta \quad (8)$$

$$S_{xy} = (S_{\parallel} - S_{\perp}) \sin \theta \cos \theta \quad (9)$$

where ρ_{\parallel} , κ_{\parallel} , and S_{\parallel} (ρ_{\perp} , κ_{\perp} , and S_{\perp}) are the thermoelectric parameters of the SmCo₅/BST multilayers in the direction parallel (perpendicular) to the stacking plane. The thickness ratio t and tilt angle θ dependences of the thermoelectric parameters for SmCo₅/BST-based ATML, which are obtained by substituting the measured properties of SmCo₅ and BST into eqn (1)–(9), are shown in Fig. 2b–d in the main text and Fig. S3.

Note S3. Influence of magnetic state on intrinsic thermoelectric performance of MCM

The magnetic state of SmCo₅ does not contribute to the transverse thermoelectric generation performance in our MCM-based module for the following reasons. Based on the transport measurement results in the magnetized and demagnetized states of SmCo₅,^{1,2} the modulation of ρ and S are 0.2% and 2.9%, respectively. Because S_{xy} of our MCM is predominantly determined by BST, the modulation of ODSE through the magnetoresistance and magneto-Seebeck effects was estimated to be less than 0.6%. The electric fields induced by the ordinary Nernst effect in BST and ANE in SmCo₅ can appear only in the cross-product direction of the x - and y -axes due to the strong magnetic anisotropy of SmCo₅ in the stacking direction (Fig. 2a in the main text) so that they are not superposed on the thermopower in the x -axis.

Note S4. Calculation of thermoelectric generation performance of MCM-based module

We calculated the ΔT dependence of V_{oc} , R_{module} , P_{max} , and conversion efficiency η of our MCM-based module using the temperature dependence of analytically calculated transverse thermoelectric properties in Fig. S4. Snyder's method^{3,4} was adopted to accurately calculate η for transverse thermoelectric conversion. By introducing the device figure of merit $Z_{xy}T$ of a transverse thermoelectric generator, η is expressed in the traditional manner as

$$\eta = \frac{\Delta T}{T_h} \frac{\sqrt{1 + Z_{xy}T} - 1}{\sqrt{1 + Z_{xy}T} + T_c/T_h} \quad (10)$$

where $\Delta T/T_h = (T_h - T_c)/T_h$ is the Carnot efficiency with $T_{h(c)}$ being the hot (cold) side temperature and the remaining factor is the reduced efficiency depending on $Z_{xy}T$. The essential difference between $z_{xy}T$ and $Z_{xy}T$ is that whereas $z_{xy}T$ is defined by $S_{xy}(T)$, $\rho_{xx}(T)$, and $\kappa_{yy}(T)$ at specific T , $Z_{xy}T$ (and η) is calculated from the temperature dependence of $S_{xy}(T)$, $\rho_{xx}(T)$, and $\kappa_{yy}(T)$ from T_c to T_h and variable with the applied load current. To exactly calculate η using $Z_{xy}T$, the temperature-dependent thermoelectric properties with an increment of 1 K were obtained by the linear interpolation and input to the spreadsheet given in the literature.⁴ Then, by taking T_h and T_c measured by the infrared camera and the dimensions and number of the MCM-elements into account, the ΔT dependence of V_{oc} and R_{module} was analytically calculated as shown in Fig. S6a,b. The relative current density u , which refers to the applied load current divided by the input heat current, was optimized to get the maximum output power P_{max} value at each ΔT value for the comparison with our experiment. Fig. S6c shows the result of the analytical calculation for P_{max} with the experimental values. The ΔT dependence of the calculated η under the same u value is shown in Fig. S6, where the η value at $\Delta T = 152$ K is estimated to be 2.4% (without any losses) and 1.6% (by multiplying the loss fraction of the measured P_{max} to the calculated one in Fig. S6c) in maximum. The corresponding normalized conversion efficiency, where η is divided by the Carnot efficiency for the fair comparison of the thermoelectric generation performance, is in the range of 5.2–7.6% in our MCM-based module. The value is much higher than that of Bi/Cu- and Ni/BST-based ATML modules (3.9% and 3.6%, respectively),^{5,6} but still lower than that of the longitudinal thermoelectric modules^{7–13} mainly due to the high thermal conductivity of our MCM. Note that the loss fraction of P_{max} can be suppressed simply by elongating the MCM element in the \mathbf{E} direction because the shunting effect at the boundaries to the electrodes predominantly decreases V_{oc} and hence P_{max} .^{14,15} Thus, the developments in both the materials performance and device engineering are significant for further improvement in η and thermoelectric applications of MCMs.

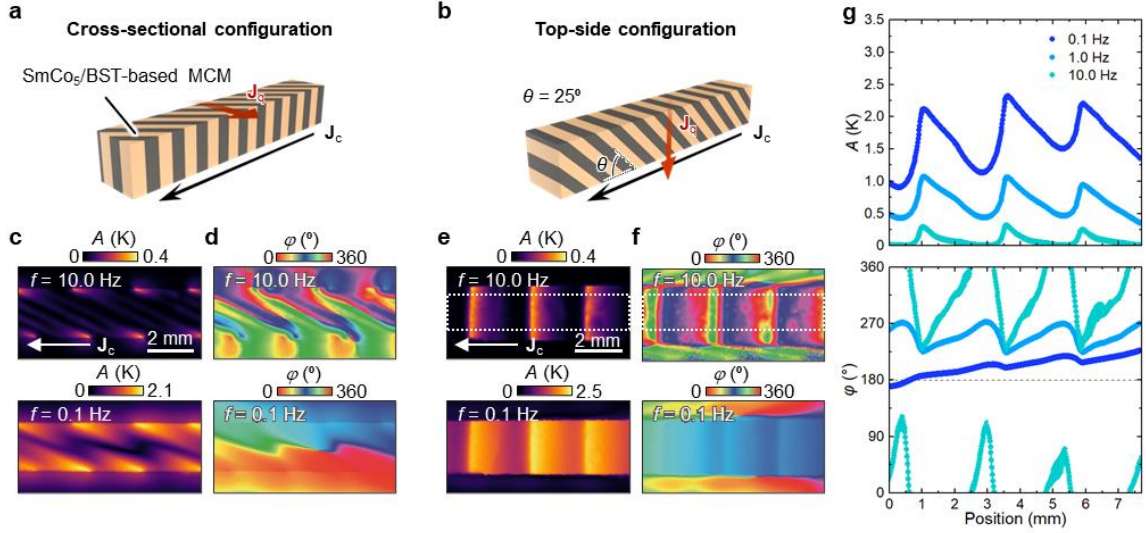


Fig. S1 Temperature modulation due to transverse thermoelectric conversion in MCM. (a,b) Schematic of the LIT measurements for MCM with $\theta = 25^\circ$ in the cross-sectional (a) and top-side (b) configurations. J_q denotes the transverse heat current generated by the off-diagonal Peltier effect in SmCo₅/BST-based MCM. (c,d) A (c) and φ (d) images in the cross-sectional configuration at $f = 10.0$ and 0.1 Hz. A (e) and φ (f) images in the top-side configuration at $f = 10.0$ and 0.1 Hz. (g) A and φ profiles along the J_c direction at $f = 0.1, 1.0,$ and 10.0 Hz for the areas defined by the white dotted rectangles with a size of 512×101 pixels in (e) and (f).

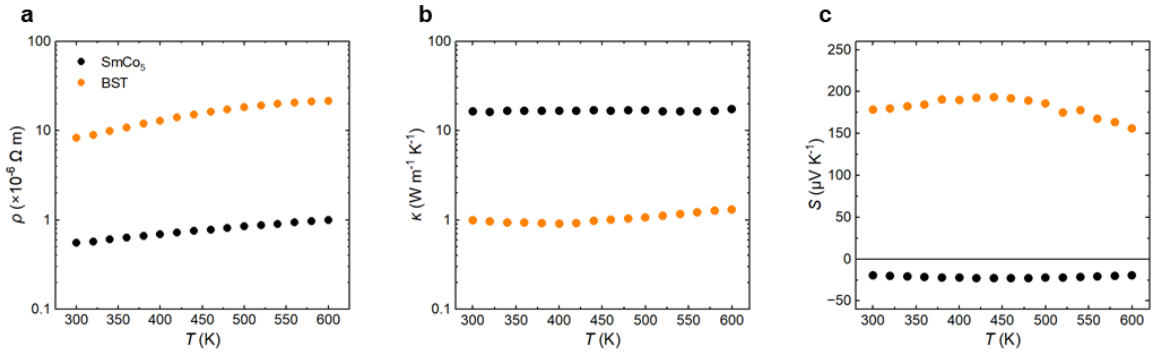


Fig. S2 Thermoelectric properties of SmCo₅ and BST. (a–c) Temperature T dependence of the electrical resistivity ρ (a), thermal conductivity κ (b), and Seebeck coefficient S (c) for the SmCo₅ and BST slabs.

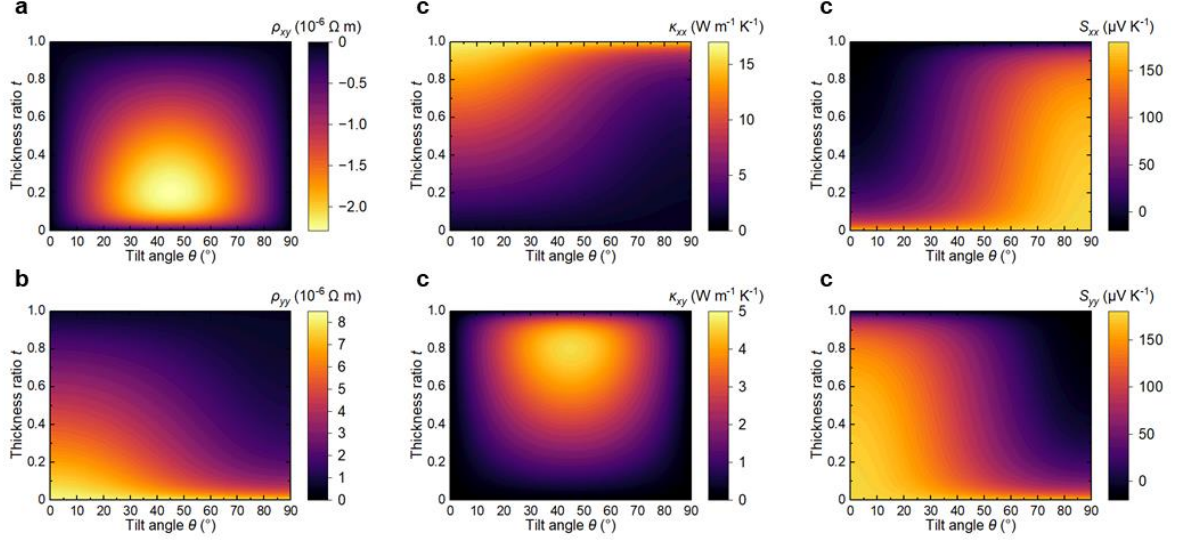


Fig. S3 (a–f) Contour plots of the analytical thermoelectric parameters ρ_{xy} (a), ρ_{yy} (b), κ_{xx} (c), κ_{yy} (d), S_{xx} (e), and S_{yy} (f) for SmCo₅/BST-based ATML.

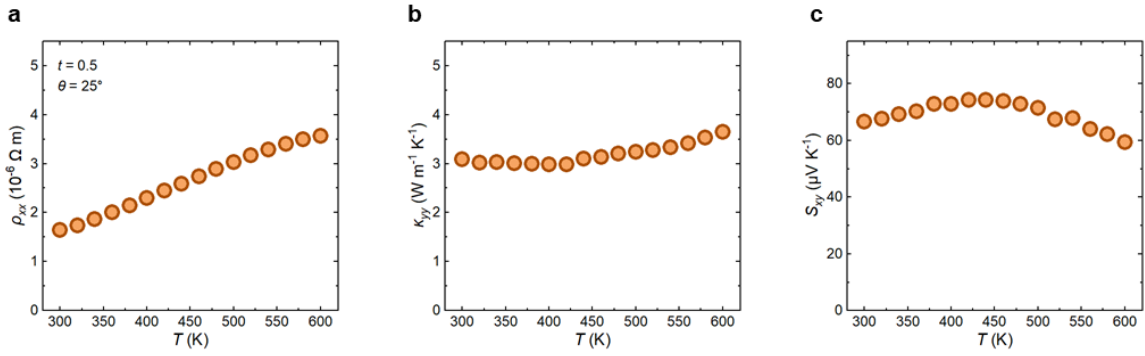


Fig. S4 (a–c) T dependence of the analytical transverse thermoelectric properties of the electrical resistivity in the x -axis ρ_{xx} (a), thermal conductivity in the y -axis κ_{yy} (b), and off-diagonal Seebeck coefficient S_{xy} (c) with thickness ratio $t = 0.5$ and tilt angle $\theta = 25^\circ$.

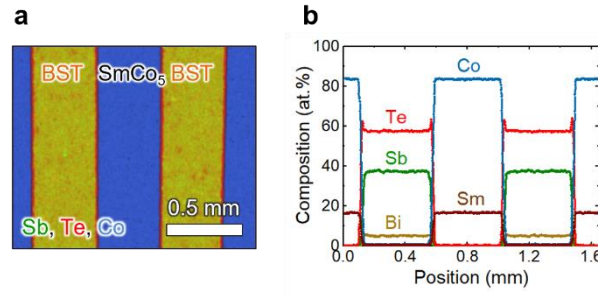


Fig. S5 Low-magnification SEM-EDX observations. (a) SEM-EDX mapping of Sb, Te, and Co for the cross section of the SmCo₅/BST multilayer. (b) Line profile of the atomic ratio of Sm, Co, Bi, Sb, and Te across the stacking direction.

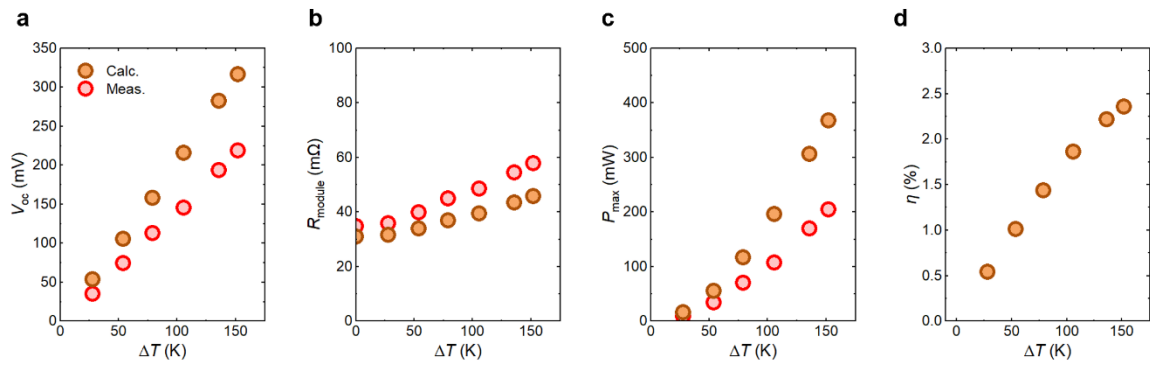


Fig. S6 Transverse thermoelectric generation performance of MCM-based module. (a–d) ΔT dependence of V_{oc} (a), internal resistance R_{module} (b), P_{max} (c), and conversion efficiency η (d) for the thermopile module composed of the 14 SmCo₅/BST-based MCM elements with $t = 0.5$ and $\theta = 25^\circ$. The orange (red) data points show the analytically calculated (experimentally measured) values. The calculated parameters are obtained by inputting the transverse thermoelectric properties based on Fig. S4 to the spreadsheet given in ref. 4.

References

- 1 K. Uchida, T. Hirai, F. Ando and H. Sepehri-Amin, *Adv. Energy Mater.*, 2024, **14**, 2302375.
- 2 A. Miura, H. Sepehri-Amin, K. Masuda, H. Tsuchiura, Y. Miura, R. Iguchi, Y. Sakuraba, J. Shiomi, K. Hono and K. Uchida, *Appl. Phys. Lett.*, 2019, **115**, 222403.
- 3 D. Michael. Rowe, *Thermoelectrics Handbook : Macro to Nano*, CRC Press, New York, 2006.
- 4 G. J. Snyder and A. H. Snyder, *Energy Environ. Sci.*, 2017, **10**, 2280–2283.
- 5 T. Kanno, K. Takahashi, A. Sakai, H. Tamaki, H. Kusada and Y. Yamada, *J. Electron. Mater.*, 2014, **43**, 2072–2080.
- 6 A. Sakai, T. Kanno, K. Takahashi, H. Tamaki, H. Kusada, Y. Yamada and H. Abe, *Sci. Rep.*, 2014, **4**, 6089.
- 7 J. R. Salvador, J. Y. Cho, Z. Ye, J. E. Moczygemba, A. J. Thompson, J. W. Sharp, J. D. Koenig, R. Maloney, T. Thompson, J. Sakamoto, H. Wang and A. A. Wereszczak, *Phys. Chem. Chem. Phys.*, 2014, **16**, 12510–12520.
- 8 G. Skomedal, L. Holmgren, H. Middleton, I. S. Eremin, G. N. Isachenko, M. Jaegle, K. Tarantik, N. Vlachos, M. Manoli, T. Kyratsi, D. Berthebaud, N. Y. Dao Truong and F. Gascoin, *Energy Convers. Manag.*, 2016, **110**, 13–21.
- 9 R. Deng, X. Su, S. Hao, Z. Zheng, M. Zhang, H. Xie, W. Liu, Y. Yan, C. Wolverton, C. Uher, M. G. Kanatzidis and X. Tang, *Energy Environ. Sci.*, 2018, **11**, 1520–1535.
- 10 Z. Liu, N. Sato, W. Gao, K. Yubuta, N. Kawamoto, M. Mitome, K. Kurashima, Y. Owada, K. Nagase, C. H. Lee, J. Yi, K. Tsuchiya and T. Mori, *Joule*, 2021, **5**, 1196–1208.
- 11 KELK Ltd., Products information on thermo generation module, <https://www.kelk.co.jp/english/generation/index.html>.
- 12 Coherent Corp., Thermoelectric Generator (TEG) Modules, <https://ii-vi.com/product/thermoelectric-generator-teg-modules/>.
- 13 Ferrotec Materials Technologies Corp., Power Generation Thermo-electric Modules, https://ft-mt.co.jp/en/product/electronic_device/thermo/power_generation/.
- 14 T. Kanno, S. Yotsuhashi, A. Sakai, K. Takahashi and H. Adachi, *Appl. Phys. Lett.*, 2009, **94**, 061917.
- 15 T. Kanno, A. Sakai, K. Takahashi, A. Omote, H. Adachi and Y. Yamada, *Appl. Phys. Lett.*, 2012, **101**, 011906.